PAPER • OPEN ACCESS

Electronic transport across extended grain boundaries in graphene

To cite this article: Arnab K Majee and Zlatan Aksamija 2021 Nano Ex. 2 030007

View the <u>article online</u> for updates and enhancements.







OPEN ACCESS

RECEIVED

19 February 2021

REVISED

4 May 2021

ACCEPTED FOR PUBLICATION

26 May 2021

2 September 2021

Original content from this work may be used under the terms of the Creative Commons Attribution 4.0 licence.

Any further distribution of this work must maintain attribution to the author(s) and the title of the work, journal citation and DOI.



PAPER

Electronic transport across extended grain boundaries in graphene

Arnab K Majee 📵 and Zlatan Aksamija 🗓

Department of Electrical and Computer Engineering, University of Massachusetts Amherst, Amherst, MA 01003-9292, United States of America

E-mail: zlatana@engin.umass.edu

Keywords: graphene, transport, grain boundary

Abstract

Owing to its superlative carrier mobility and atomic thinness, graphene exhibits great promise for interconnects in future nanoelectronic integrated circuits. Chemical vapor deposition (CVD), the most popular method for wafer-scale growth of graphene, produces monolayers that are polycrystalline, where misoriented grains are separated by extended grain boundaries (GBs). Theoretical models of GB resistivity focused on small sections of an extended GB, assuming it to be a straight line, and predicted a strong dependence of resistivity on misorientation angle. In contrast, measurements produced values in a much narrower range and without a pronounced angle dependence. Here we study electron transport across rough GBs, which are composed of short straight segments connected together into an extended GB. We found that, due to the zig-zag nature of rough GBs, there always exist a few segments that divide the crystallographic angle between two grains symmetrically and provide a highly conductive path for the current to flow across the GBs. The presence of highly conductive segments produces resistivity between 10^2 to $10^4 \Omega \mu m$ regardless of misorientation angle. An extended GB with large roughness and small correlation length has small resistivity on the order of $10^3 \Omega \mu m$, even for highly mismatched asymmetric GBs. The effective slope of the GB, given by the ratio of roughness and lateral correlation length, is an effective universal quantifier for GB resistivity. Our results demonstrate that the probability of finding conductive segments diminishes in short GBs, which could cause a large variation in the resistivity of narrow ribbons etched from polycrystalline graphene. We also uncover spreading resistance due to the current bending in the grains to flow through the conductive segments of the GB and show that it scales linearly with the grain resistance. Our results will be crucial for designing graphene-based interconnects for future integrated circuits.

1. Introduction

Over the last 50 years, persistent scaling of transistors in integrated circuits has been accompanied by shrinking the dimension of interconnects and vias, typically made of copper. Current state-of-the-art uses polycrystalline copper interconnects as thin as 10 nm. However, due to the increased surface roughness and grain boundary (GB) scattering, the resistivity of copper increases exponentially below 100 nm, which imposes a limit to further downscaling of copper interconnects [1]. This limitation has led to extensive research in finding a suitable alternative that can replace copper in the next-generation nanoelectronic devices and circuits. Owing to the ultrathin nature and superior carrier mobility, monolayer graphene is envisioned as a promising candidate for interconnects and contacts in the emerging integrated circuits [2–4]. The dimension of mechanically exfoliated single-crystalline graphene samples are limited to few tens of microns whereas commercial integration of graphene requires wafer-scale manufacturing. Currently, chemical vapor deposition (CVD) on metal substrates is the most commonly used technique to grow such large-area 2D sheets [5–8]. Controlled growth and nucleation processes using low-pressure CVD, adjusting content of oxygen on the surface of Cu substrate, and replacing methane with ethanol as carbon source have yielded single crystals up to a centimeter [5, 9, 10] and films up to 30 inches [11] in dimension.

nanometer-scale roughness.

CVD-grown graphene is inherently polycrystalline in nature. It consists of grains of various sizes and random crystallographic orientations, where every pair of adjacent grains are separated by a GB. The difference in crystallographic orientation between adjacent grains—referred to as misorientation angle Θ_M —results in mismatch in the crystal structure at their junction. Based on substrate imperfections and other factors governing the growth process, GBs may contain topological defects [12–14] and have wrinkles of varying width up to 20nm [8, 15, 16]. In general, GBs were found to limit electrical performance of graphene transistors [17]. Several experimental studies [18–20] have been carried out to understand the effect of Θ_M on electrical transport properties in graphene. The resistivity of individual GB (ρ_{GB}) varies over a narrow range—few hundred Ω μ m [15, 21, 22] to several tens of k Ω μ m [22–24] and shows no clear correlation with Θ_M . Imaging GBs using optical [25], scanning electron [26] and high resolution scanning transmission electron microscopes [27, 28] reveals that GBs are straight lines only at the microscopic scale, up to a few nanometers. Typically, the average length of the GB scales with grain diameter and may extend from few tens of nanometers to several microns. Over this mesoscopic length scale, GBs are rarely straight lines; rather, they meander between two grains [27], exhibiting

In contrast to experimental findings, several theoretical studies have investigated the effect of Θ_M on graphene ρ_{GB} and predicted a strong correlation between them [29–32]. These studies revealed the opening of a transport energy gap [30], which is a consequence of the simultaneous energy and momentum conservation of a quantum-mechanical wave traveling across an interface [33]. The size of the transport gap depends on Θ_M and the symmetry of the GBs. Consequently, ρ_{GB} varies very strongly with the size of the transport gap as the number of carriers contributing to transport depends exponentially on the gap size. It has also been shown that ρ_{GB} not only depends on the total Θ_M , but exhibits a strong dependence on the degree of asymmetry of GBs which is given by the relative angles between the boundary and the crystallographic orientations of each grain. In asymmetric GBs with large Θ_M , the transport gap is so large that ρ_{GB} is 20 orders of magnitude greater than those with small Θ_M [32]. These theoretical studies investigated electronic transport across GBs only up to a few nanometers in length; as a result, they assumed GBs to be straight lines [34]. But a nanometer-long straight line is representative of only a small section of the actual (experimentally-observed) GBs, which are typically micronlength. Consequently, the prediction of the ρ_{GB} deviates significantly from experimental measurements. To distinguish between the previous theoretical studies where researchers have investigated electronic transport across a small section of the GB, we refer to the entire GB as extended GB. Since GBs are not straight lines, we have used here the term non-straight GBs interchangeably with extended GBs. There has not been any attempt made, so far, to examine the impact of roughness and zig-zagness on the resistivity of extended graphene GBs.

Here we study electronic transport across and in the vicinity of extended GBs, for which we developed a novel two-step approach. The first step is to use a generalized autocorrelation function to generate self-affine 1D boundaries with a given rms roughness Δ and lateral correlation lengths L_{corr} . Next, we employed a method developed in our previous work [32] to calculate the transmission of charge carriers across each GB segment based on simultaneous energy and momentum conservation and extended it to study transport across these non-straight GBs. Our results clearly show that the meandering nature of a GB yields a few highly conductive GB segments. The conductive segments are found to be the ones which bisect the relative crystallographic angles of the grains constituting the boundary. Consequently, the overall resistivities of extended GBs fall within a universal range of 10^2 to $10^4 \Omega \mu m$, irrespective of the misorientation angles. This range of resistivity values aligns quite well with those measured experimentally. We show that the ρ_{GB} is inversely proportional to the effective slope of the GB, given by Δ/L_{corr} . In the second step, we study the effect of spreading resistance on electrical transport in graphene samples with extended GBs. The method uses a 2D Voronoi tessellation (VT) to emulate an extended GB and simultaneously discretize the grains on both sides of the GB into small simulation cells. Then we iteratively solve for current conservation in each discretized Voronoi cell to obtain a steady-state voltage profile. Our results corroborate that even in the presence of grain resistance, most voltage drop occurs near the GB. The resulting current curves and is forced to travel an additional path in the graphene grain to reach the few conductive segments of the GB, giving rise to a spreading resistance, which we found to be directly proportional to the resistance of the graphene grains.

2. Methodology

2.1. Simulation of non-straight GBs

In the past, researchers have generated 2D self-affine surfaces from their autocorrelation functions for the purpose of understanding the effect of surface roughness on several physical properties of materials [35–37]. Here we used a generalized autocorrelation function of the form [38]

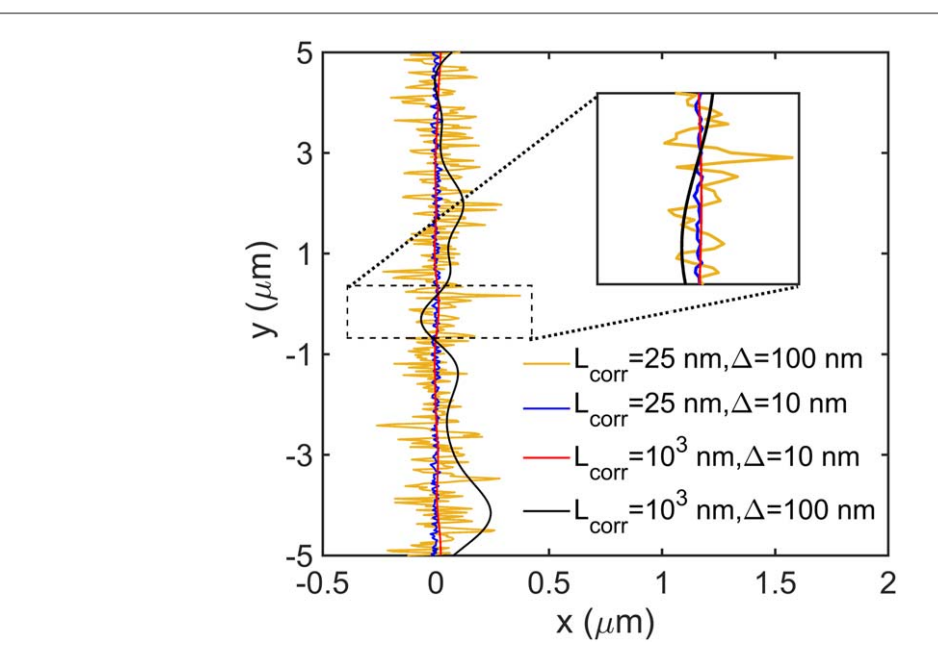


Figure 1. Shows non-straight GBs with different rms roughness (Δ) and correlation lengths (L_{corr}). The red and blue lines represent highly correlated and uncorrelated GBs, respectively, with small Δ , whereas the black and yellow curves represent GBs with large Δ for L_{corr} equal to 1000 and 25 nm, respectively. The inset shows a zoomed-in view of the various non-straight GBs.

$$C(x) = \Delta^2 \exp\left[-\left(\frac{|x|}{L_{corr}}\right)^{2H}\right]$$
 (1)

to generate non-straight GBs with a given rms roughness (Δ) perpendicular to and correlation length (L_{corr}) along the GB. Several natural surfaces used in various engineering applications are shown to exhibit a Hurst exponent (H) greater than 0.7 [39]. The values of H can in general vary between 0 and 1, where higher values represent rough lines with less jagged peaks. We have used H = 1, where peaks resemble Gaussian curves, here in this study to simulate extended boundaries. Then we calculated the power density spectrum S(q) from the Fourier transform of the autocorrelation function $S(q) = \mathcal{F}[C(x)]$. To generate correlated lateral deviations (h) from a straight line for a range of x, we first multiply the square root of S(q) with a random phase $e^{i\phi}$, generated by taking Fourier transform of a set of randomly distributed points, and then take an inverse Fourier transform of the product as

$$h(x) = \mathscr{F}^{-1}[\sqrt{S(q)}e^{i\phi}]. \tag{2}$$

Figure 1 shows 10 μ m-wide GBs with different L_{corr} and Δ generated from equation (2). The yellow and blue curves are for a small correlation length ($L_{corr}=25$ nm) and different rms roughness (100 and 10 nm, respectively), whereas the black and red lines correspond to GBs with large correlation length ($L_{corr}=1$ μ m) and Δ equal to 100 and 10 nm, respectively. The inset shows a zoomed view of a region for these GBs. The regions on the left and right-hand side of the GB are the two grains with crystallographic angles of x° and y°, respectively, referenced to the y-axis, such that x° + y° = Θ_M . Each GB segment makes a different angle with the crystal orientation of the left and right grains, which we refer here as Θ_L and Θ_R , respectively.

2.2. Calculation of GB resistivity

To compute the resistivity of the entire GB, we first calculate the resistivity of each segment corresponding to the pair of angles, Θ_L and Θ_R , based on an approach developed in our previous work [32]. In this approach, we calculate the electronic bandstructure of monolayer graphene from first principles based on Density Functional Theory using the open-source software Quantum ESPRESSO [40]. Then we compute a mode-dependent transmission coefficient based on quantum-mechanical wave continuity [33]. From translational symmetry, transmission requires simultaneous conservation of energy and transverse momentum of the incident electron across the GB. Momentum conservation requires that the parallel component of the incident wave vector $k_{i_{\parallel}}$ be equal to the parallel component of the transmitted wave vector $k_{t_{\parallel}}$ in their respective domains, that is $k_{t_{\parallel}} = k_{i_{\parallel}}$. Simultaneously, energy is conserved by finding a perpendicular component of the transmitted wave vector $k_{t_{\perp}}$, within the first Brillouin zone of the right grain, such that $E_2(k_{t_{\parallel}} + k_{t_{\perp}}) = E_1(k_i) = E_1(k_{i_{\parallel}} + k_{i_{\perp}})$. We calculate the mode-dependent transmission coefficient $\tau_b(\vec{k})$ for each band b using the perpendicular components of the incident $k_{t_{\perp}}$ and transmitted $k_{t_{\perp}}$ wave vectors according to the expression

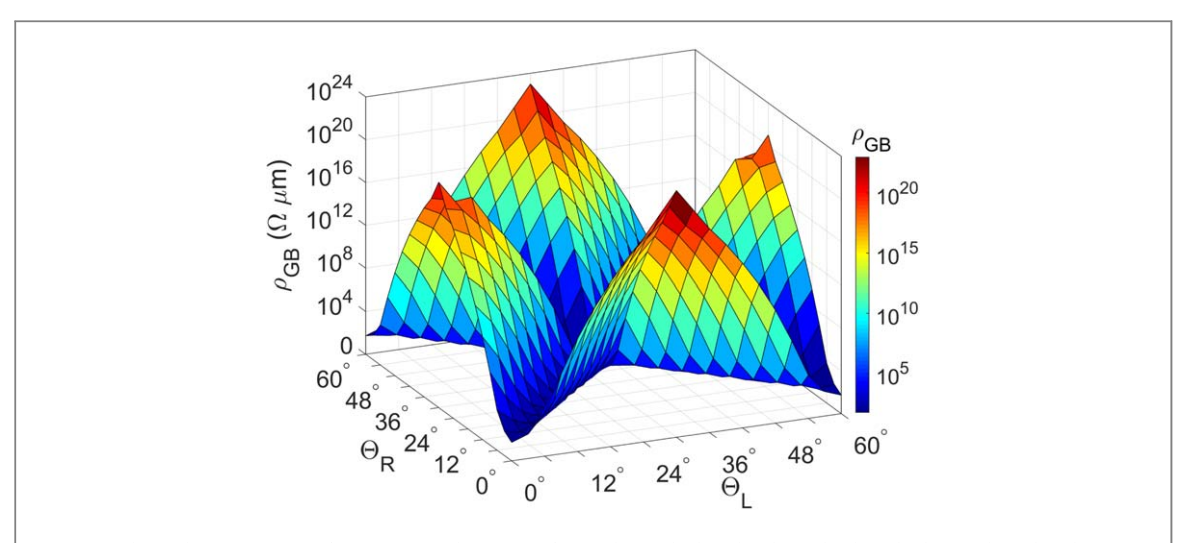


Figure 2. Shows the resistivity ρ_{GB} for various combinations of Θ_L and Θ_R , which is also shown by the color bar on the right. The regions with blue color represents low resistivity and red color stands for high resistivity.

$$\tau_b(k_i) = \frac{|4k_{i_\perp}k_{t_\perp}|}{|k_{i_\perp} + k_{t_\perp}|^2}.$$
 (3)

Next, we obtain the band- and energy-resolved transport distribution function (TDF) $\Xi_b(E)$ by integrating the mode-dependent transmission coefficient $\tau_b(k)$ over the constant energy contour, described by $\delta(E-E_b(k))$, using a 2D version of the linear extrapolation approach [41] as

$$\Xi_b(E) = \frac{1}{4\pi^2} \int \tau_b(k_i) \delta(E - E_b(k_i)) dk_i, \tag{4}$$

Finally, the conductivity of the GB segment is obtained from the sum of TDFs over all the bands in the Landauer formalism as

$$G_{GB}^{i} = \frac{e^{2}}{2} \int_{E_{C}}^{E_{max}} \Xi(E) \left(-\frac{\partial f(E - E_{F}, T)}{\partial E} \right) dE, \tag{5}$$

where f(E) is the Fermi–Dirac distribution function $f(E) = [1 + \exp((E - E_F)/k_BT)]^{-1}$. The corresponding resistivity of the GB segment, ρ_{GB}^i , is obtained by taking the reciprocal of the G_{GB}^i . Further details of the theoretical approach to compute resistivity of the segment can be found in our previous work [32].

We used a carrier density of 6×10^{12} cm⁻² as a typical value representative of experimental samples to compute ρ_{GB}^i . The dependence of ρ_{GB}^i on any combination of Θ_L and Θ_R is summarized in figure 2. Symmetric segments ($\Theta_L = \Theta_R$) exhibit the smallest resistivity on the order of $10^2 \Omega$ μ m, whereas asymmetric segments show orders of magnitude higher resistivity due to the opening of a transport gap [29–32]. Since all segments making up a GB are parallel channels for the current, the overall GB conductance is given by the sum of conductances of all the segments, $G_{GB} = \Sigma_i L_{GB}^i / \rho_{GB}^i$, where L_{GB}^i represents the length of each GB segment. Then the GB resistivity is calculated as $\rho_{GB} = L_{GB}/G_{GB}$, where L_{GB} is the length of the GB. The method discussed above computes the ballistic resistance across any non-straight GB with given Δ , L_{corr} , \mathbf{x}° and \mathbf{y}° . To get a complete picture of electron transport across a graphene sample with GB, it is essential that we obtain the voltage profile between two contacts where both grains and the GB are present simultaneously in the calculation. In the second step, we developed a novel approach using a 2D tessellation to emulate a non-straight GB while also using it as a tool to discretize the grains.

2.3. Calculation of steady-state current and voltage

The Voronoi tessellation (VT) has been widely used in the past to emulate the microstructure of polycrystalline materials for both 2D [42] and three-dimensional materials [43]. Here we employ a 2D VT to mimic grains separated by non-straight GBs. The 2D VT starts with a set of points, called seed points, randomly distributed in a 2D plane with a uniform distribution. The space is then divided into subspaces, called Voronoi cells (VC), around each seed point by bisecting the lines connecting each seed point with its nearest neighbors and assigning the smallest space enclosed by the bisecting lines to the VC, such that all the space inside any given VC is closer to the seed point associated with it than any other seed point. In other words, these seed points are the centroids (centers of mass) of their respective VCs and hence this method is also called centroidal Voronoi tessellation. The number of Voronoi cells that is generated equals the number of seed points. The network of non-overlapping polygons thus formed is shown in figure 3. The Voronoi cells are grouped to form two grains. The

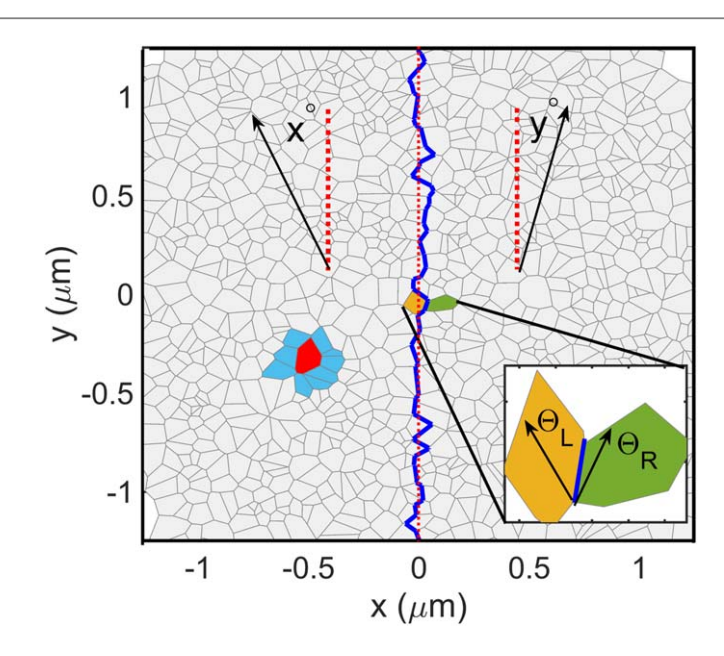


Figure 3. Voronoi diagram obtained from 2D VT. All the VCs on the left of the GB, traced by the solid blue line, form the left grain and the ones on the right side constitute the right grain. The left and right grains are taken to have crystal orientations at angles x° and y° , respectively, measured with respect to the y-direction. The orientations of the left and right grains relative to a segment of the GB is given by Θ_L and Θ_R , shown in the inset.

left grain is comprised of all the Voronoi cells whose centers are located on the left of the red-dotted middle line, which bisects the Voronoi diagram laterally. The right grain consists of the remaining Voronoi cells, whose centers are located on the right of the red-dotted line. The zig-zag line separating the two grains forms a non-straight GB, as shown by the blue line in figure 3. Then we calculate the local orientations of each GB segment with respect to the orientations of the left and right grains, indicated by Θ_L and Θ_R , respectively, as shown in the inset of figure 3. Then we follow a similar approach as described in section 2.2 to compute the GB resistivity.

In order to solve for the voltage distribution in the grains surrounding a GB, we developed an iterative procedure. Under the steady-state conditions, the net current flowing in and out through the edges of each Voronoi cell must be zero. Mathematically,

$$\sum_{i} I_{ij} = 0, \forall i, \tag{6}$$

where the index j represents the first neighboring VCs, shown in blue in figure 3, of the i-th cell, depicted as the red cell in figure 3. The current flowing out of the i-th VC I_{ij} is calculated as $(V_i - V_j)G_{ij}$, where G_{ij} is the conductance between cells i and j. The resistance R_{ij} (reciprocal of G_{ij}) comprises of the total resistance between i-th and j-th VCs. The resistance is determined from $R_{ij} = (\rho_{grain} \times L_{ij}/W_{ij}) + R_{ij}^{GB}$, where ρ_{grain} is the sheet resistance of single-crystalline graphene, which depends on the mobility and carrier density. L_{ij} is the distance between i-th and j-th cells and W_{ij} is the length of the edge separating the two VCs. If cells i and j are on either sides of the GB, then R_{ij}^{GB} is the resistance of the specific GB segment separating them; otherwise, it is set to zero for all the cells in the interior of the grains.

On substituting $I_{ij} = (V_i - V_j) \times G_{ij}$ in equation (6) and rearranging the terms, V_i can be written as $V_i = \sum_j V_j \times G_{ij} / \sum_j G_{ij}$. Then we set up an iterative loop, where we updated the voltages of each Voronoi cell based on the voltages of its neighbors from the last iteration as

$$V_i^{n+1} = \frac{\sum_j V_j^n \times G_{ij}}{\sum_j G_{ij}}.$$
 (7)

A voltage of 1 V was applied in a region on the left side of the sample shown in figure 3 and a region on the extreme right of the sample is held grounded. Then we iteratively updated the voltage of all the Voronoi cells to compute the steady-state current flowing through the entire simulated domain. Steady state is reached when the maximum voltage change of all the cells between two consecutive iterations is less than 10^{-4} %, which took about 5000 iterations in most cases.

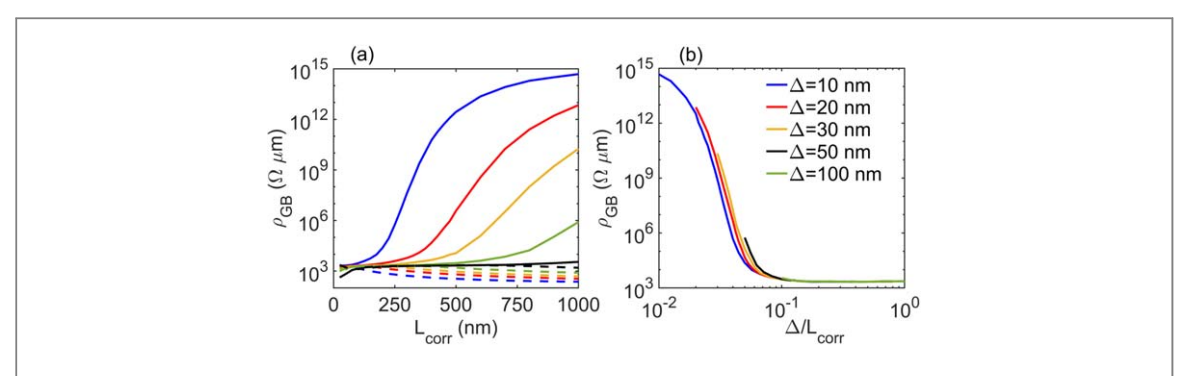


Figure 4. (a) Shows the dependence of ρ_{GB} on the roughness and correlation length of non-straight GBs. The same data for ρ_{GB} is plotted against the average slope of the GB in (b), showing that all GB resistivities follow a universal dependence.

3. Results and discussion

3.1. Resistivity for GBs with different roughness and correlation length

We focus here on the effect of structure of non-straight GBs on their resistivity, especially for asymmetric GBs with large Θ_M ; for demonstration, we used a highly asymmetric case of $(x^\circ, y^\circ) = (0^\circ, 20^\circ)$. We used roughness and correlation length to characterize the structure of extended GBs. In figure 4(a), we found that the resistivity is lowest for GBs with the largest Δ and the smallest L_{corr} , which is counter-intuitive because roughness and short correlation lengths are often associated with adverse effects on transport. Since the conductivity of a non-straight GB depends on the probability of finding a symmetric segment, a more wavy GB, which is caused by large roughness and small correlation length, exhibits the smallest resistivity, as we can see in figure 4(a). Small correlation length and large roughness corresponds to a GB with steep effective slope. Figure 4(b) shows the GB resistivity for the same set of correlation length and roughness but plotted against the slope of the GB, given by the ratio Δ/L_{corr} . We found that GB resistivity is inversely proportional to the slope with ρ_{GB} showing an universal trend for all combinations of correlation length and roughness, which indicates that the average slope of a GB can be used as a universal quantifier for the GB resistivities. The resistivity of a symmetric, non-straight GB shows negligible dependence on roughness and correlation length, as shown by the dashed lines in figure 4(a).

Next, we explored the effect of misorientation angles on resistivity of non-straight GBs. In figure 5(a), solid lines represent the most asymmetric cases $(0^{\circ}, \Theta_M)$ and dashed lines are for symmetric ones $(\Theta_M/2, \Theta_M/2)$. For asymmetric GBs, when the effective slope of the GB (Δ/L_{corr}) is large (blue and yellow solid lines), the GB resistivity varies between 10^2 to $10^4 \Omega \mu m$ and is more or less independent of the misorientation angle, especially for $\Theta_M > 5^{\circ}$. Our results show that the zig-zag nature of GBs makes them orders of magnitude more conductive than the straight line ones. An extended GB with small Δ and large L_{corr} would resemble a straight-line GB. We calculated the resistivity for GBs with Δ and L_{corr} equal to 10 and 500 nm, respectively, (green curves) for various misorientation angles to compare the results with those of the straight line GBs published in our previous work [32]. We found that the solid green curve shows a strong dependence on Θ_M and the resistivity values range from a few hundreds to 10^{20} Ω μ m, similar to those of the black square markers, which show the resistivity versus Θ_M for asymmetric, straight line GBs. On the other hand, the green dashed line shows a similar trend as the resistivities of straight line GBs for symmetric case, which is shown here by black circular markers. For symmetric cases, the resistivities of uncorrelated boundaries with different roughness show slightly higher values than those of the straight line ones, but the resistivity values are still quite small, varying between 1000 to 2000 Ω μ m. In short, due to the waviness of GBs, there always exist a few segments which provide a conductive path for the current to flow across a GB, and as a result, the resistivity of most experimentally-observed (non-straight) GBs exhibits negligible dependence on misorientation angle. Our results corroborate with the work of Tapasztó et al [44], where they used scanning tunneling microscopy to map the local conductivities of graphene GBs and found a non-uniform conductivity across various regions of a GB.

To identify the conductive segments in a non-straight GB, we plotted the resistivity of each segment ρ_{GB}^i against the angles Θ_i that each segment makes with a vertical reference axis for various Θ_M shown by different colors in figure 5(b), where red, black, yellow, blue and green curves correspond to Θ_M equal to 5°, 10°, 15°, 20°, and 25°, respectively. We found that only a few segments have resistivity as small as $10^2 \Omega \mu m$, whereas remaining segments are highly resistive. To further probe into the most conductive segments of the GB, we plotted ρ_{GB}^i versus $\Theta_L - \Theta_R$ in figure 5(c). We found that the segments with $\Theta_L - \Theta_R$ equal to zero have the smallest resistivity; $\Theta_L - \Theta_R$ equal to zero corresponds to segments that divide the crystallographic angles of the grains symmetrically. When $|\Theta_L - \Theta_R|$ increases, the resistivity of those segments also increases exponentially;

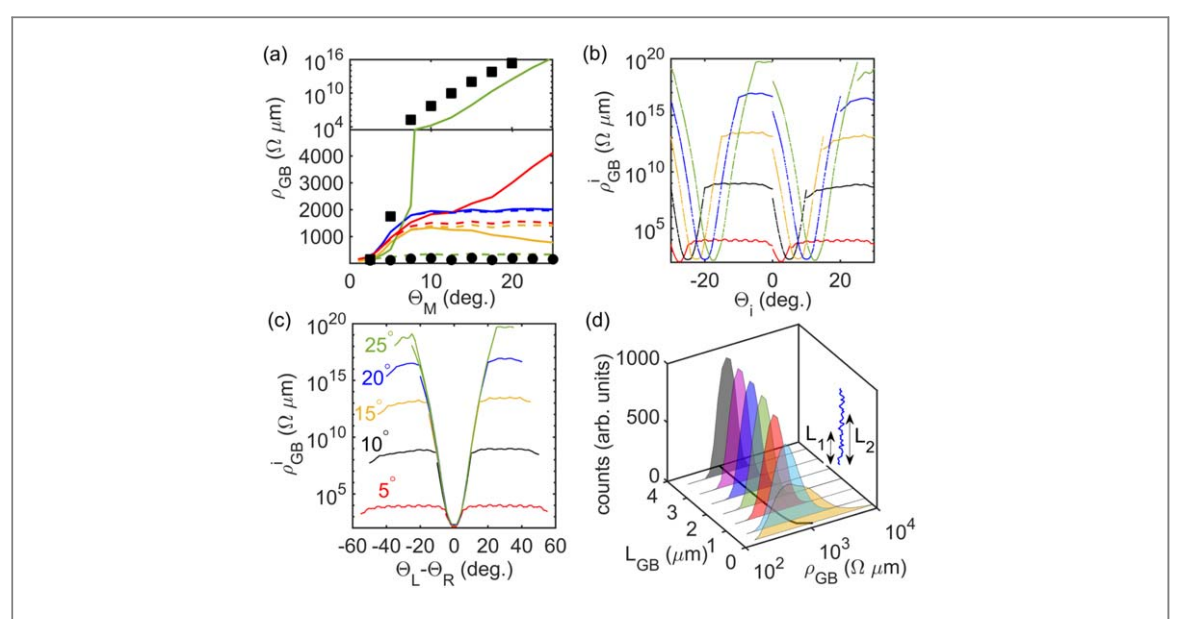


Figure 5. (a) Shows the resistivity of non-straight line GBs versus misorientation angle Θ_M for various correlation length and roughness values. The solid and dashed lines represent resitivities of asymmetric and symmetric GBs, respectively. (b) shows the resistivity of each GB segment ρ_{GB}^i versus the angles (Θ_i) that each segment makes with a vertical reference axis for various Θ_M . Red, black, yellow, blue and green curves correspond to 5° , 10° , 15° , 20° , and 25° , respectively. Segments with Θ_i equal to $\Theta_M/2\pm30^\circ$ divide the crystallographic angles of the grains symmetrically and will exhibit the smallest resistivity. This is illustrated in (c) where the resistivity of each segment is plotted against the relative difference between the crystallographic angles of each grain with Θ_i given by $\Theta_L - \Theta_R$; the segments with the smallest $|\Theta_L - \Theta_R|$ has the least resistivity and as $|\Theta_L - \Theta_R|$ increases exponentially. (d) shows the distribution of resistivity of 5000 GBs as a function of the length of the GB, as shown by different colors: 200 nm (yellow), 600 nm (cyan), 1.2 μ m (red), 1.8 μ m (green), 2.4 μ m (blue), 3 μ m (magenta) and 3.6 μ m (black).

consequently, we found that only those segments with $|\Theta_L - \Theta_R| < 5^{\circ}$ contributes to the overall conductance of the GB and a higher probability of finding such segments would lead to smaller GB resistivity.

Since interconnects made of narrow graphene ribbons are obtained by etching sections of a large CVD-grown graphene sheet, the likelihood of finding conductive segments would depend on the length of the GBs. To analyze the chance of finding conductive segments as a function of the length of the GB, we simulated 5000, 4 μ m-long GBs. Then we cut sections from each GB of varying lengths as shown in the inset of the figure 5(d). Then we plotted a smoothed histogram showing the distribution of resistivities for 5000 GBs for each length shown by different colors—200 nm (yellow), 600 nm (cyan), 1.2 μ m (red), 1.8 μ m (green), 2.4 μ m (blue), 3 μ m (magenta) and 3.6 μ m (black). All the GBs have Δ and L_{corr} equal to 50 nm and 25 nm, respectively, and the crystallographic angles of the two grains on either sides of the GB are 0° and 20°. We can clearly see that the GBs shorter than 1 μ m exhibit large variation in resistivities, and as the length of the GB increases the width of the distribution gets tighter indicating smaller variations in resistivities. The statistical mean of GB resistivity for each length is represented by the black line on the xy-plane of figure 5(d). The average resistivity decreases with the increase in the GB length up to 1 μ m and then shows negligible change with increasing length. Figure 5(d) indicates that the shorter the GB, the lower is the likelihood to find conductive segments, which in turn, translates to larger variation in their resistivities. This can have a significant impact on the variability in the resistance of narrow interconnects made from CVD-grown graphene.

While controlling the shape and structure of the GBs in 2D materials is still in rudimentary stages, the ability to engineer GBs with large roughness and small correlation length, that is GBs with highly zig-zag nature, would yield more uniform resistivities in samples/interconnects made up of polycrystalline graphene. Since our results show that there is negligible variability in resistivities in graphene strips with wide-GBs, we recommend that interconnects are patterned in such a way to keep the GBs in the wider regions/contacts and out of the narrow strips that reach individual devices.

3.2. Spreading resistance

Lastly, we turn to the path of current near the GB and examine the effect of the large variation in resistivity along the GB on current flow. Figure 6(a) shows the steady-state voltage profile in a 2.5 μ m \times 2.5 μ m sample with an asymmetric GB at x=0. The crystal orientations of left and right grains are 0° and 20° , respectively. We used a carrier density of 6×10^{12} cm⁻² to calculate the GB and grain resistances. A mobility of 100 cm² V⁻¹ s⁻¹ is used here to compute the sheet resistance of graphene grains. The conductance of the GB segments is qualitatively represented here by a color scheme shown on the right of the figure. The highly resistive segments are depicted by black lines, and the light-colored segments are the conductive ones. The two most conductive segments of the

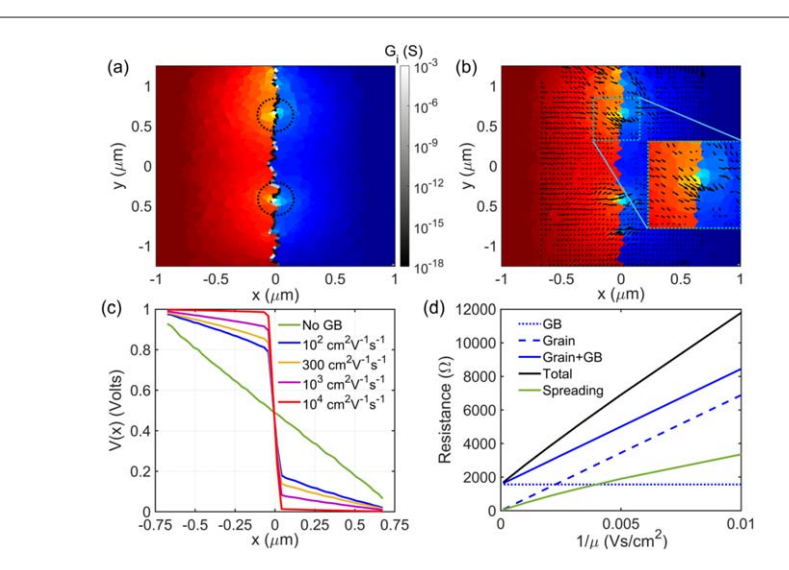


Figure 6. (a) Shows the steady-state voltage profile between the two contacts in a 2.5 $\,\mu\mathrm{m} \times 2.5\,\mu\mathrm{m}$ graphene sample with a GB at $\mathrm{x}=0$. The conductivity of each GB segment is represented by color (colorbar on the right). The two most conductive segments of the GB are encircled in the figure. (b) direction and magnitude of the current flowing through the sample is shown by the direction and length of the arrows, respectively. The inset shows a zoomed-in image of the region in the vicinity of the most conductive segment, where current-crowding to access the conductive segment of the GB occurs. (c) shows the average voltage profile along the x-direction for various grain resistances ($\infty\mu^{-1}$). (d) shows the variation of the total and spreading resistance as a function of the grain's inverse mobility.

GB are encircled in figure 6(a). For the contacts, a fixed voltage of 1V (shown by dark red) is applied in the region $-1 < x < -0.75 \ \mu m$, whereas the region on the right, $0.75 < x < 1 \ \mu m$, is grounded (shown by dark blue). The smooth transition in the voltage profile from red to blue near the conductive segments corroborates that majority current flows through a few narrow segments of a GB. The current flow in the grains and across the GB is shown by arrows overlaid on the top of the voltage profile shown in figure 6(b). The magnitude and direction of the current flow is represented by the length and direction of the arrows, respectively. We can see here that the current curves near the GB to access the most conductive segments. Also, the magnitude of the current is largest around the conductive GB segments, which is shown in the inset of figure 6(b).

To determine the potential drop along the length of our simulation domain, we calculated an average voltage, shown by the blue line in figure 6(c), in the x-direction, $V(x) = \frac{1}{L_y} \int V(x, y) dy$, where L_y is the width of the sample. We see that about 65% of the applied voltage drops across the GB. The green curve in figure 6(c) represents voltage drop in a sample without GB, where the potential drops linearly along the sample, as expected. Since the conductance of a single-crystalline graphene varies between a wide range depending on the impurities, defects and other fabrication parameters, we plotted V(x) along the sample for different grain resistance, R_{grain} , which we tuned by varying mobility between 10^2 to 10^4 cm² V⁻¹ s⁻¹. We see that in a sample where the mobility is as high as 10^4 cm² V⁻¹ s⁻¹, more than 95% of the voltage drops at the GB; in such samples one can approximate the resistance of the entire sample by the R_{GB} only.

The effect of current curving and traversing additional path in the grain to access the conductive channels of a highly resistive GB is typically represented by spreading resistance R_{spread} , such that the total resistance can be decomposed into $R_{tot} = R_{grain} + R_{GB} + R_{spread}$. Figure 6(d) shows the spreading resistance as a function of the grain resistance, which is proportional to the $1/\mu$, as the dashed blue line. The total resistance of the sample, which is calculated from the voltage difference between the two contacts divided by the total steady-state current passing through the GB, is shown by the black curve. We can see that R_{tot} is equal to $R_{GB} + R_{grain}$ (shown by the solid blue line) when the grains are highly conductive, that is $\mu=10^4\,{\rm cm^2\,V^{-1}\,s^{-1}}$. When the resistance of the grains $(\propto \mu^{-1})$ increases, the difference between the R_{tot} and $R_{GB} + R_{grain}$, which is the spreading resistance as shown by the green curve, also increases. In other words, we found that the current curves more to flow through the conductive GB segments in more resistive grains. As a result, the current flow is non-uniform along the GB; the degree of non-uniformity is captured by the spreading resistance. We also found that the current flowing out of a narrow conductive GB segment qualitatively resembles a cylindrical current source in 3D [45]. Since graphene is two-dimensional, the voltage profile inside each grain would approximately follow a circular solution of the form $V(L) \propto I \rho_{sheet} \times \frac{1}{2} \ln(\frac{L}{2l_{GB}})$ for $l_{GB} \ll L/2$ as the current spreads radially into or out of a narrow conductive segment. Here L is the distance between the two contacts and l_{GB} is the effective length of the conductive segment. We calculated an effective length of the conductive segment, $\sum_i G_i L_i / \sum_i G_i$, to be about 30 nm, which is only 1.2% of the total length of the GB.

4. Conclusions

Our novel two-step simulation of rough extended GBs uncovered that, due to the zigzag nature of extended GBs, a few segments of the GB divide the relative crystallographic angles between two grains symmetrically, which makes these segments highly conductive. The presence of such conductive segments weakens the correlation between the resistivity and misorientation angles that was reported in previous theoretical studies of short linear GBs. The resistivity of non-straight GBs are found to be independent of misorientation angles and lie in an universal range of 10^2 to $10^4 \, \Omega \, \mu$ m. Our findings bridge the discrepancy between experiments and previous theoretical reports. Since the probability of finding conductive segments is higher when Δ is large, we found that resistivity is inversely proportional to the average slope (Δ/L_{corr}) of the GB. As a result, extended GBs with large roughness and small correlation length exhibit the least resistivity. The steady-state voltage profile of a graphene sample with extended GB shows that the current bends in the grains to flow through the few conductive segments, which gives rise to a spreading resistance. We found that the spreading resistance scales linearly with the grain resistance.

Due to the lower probability of finding conductive segments, short GBs exhibit a broader distribution of resistivities, which may increase variability in interconnects made of narrow graphene ribbons. While controlling the shape and structure of the GBs in 2D materials is still in rudimentary stages, the ability to engineer GBs with large roughness and small correlation length, that is GBs with highly zig-zag nature, would yield lower and more uniform resistivities in samples/interconnects made up of polycrystalline graphene. Since our results show that there is negligible variability in resistivities in wide graphene ribbons with GBs, we recommend that graphene is patterned in such a way to constrain the GBs to the wider regions such as contacts and out of the narrow strips that reach individual devices in order to achieve minimal variability. Beyond improving our understanding of electrical transport across extended GBs in polycrystalline monolayers, this study will guide engineers in designing graphene interconnects for future nanoelectronic integrated circuits.

ORCID iDs

Arnab K Majee https://orcid.org/0000-0002-0780-7486 Zlatan Aksamija https://orcid.org/0000-0001-9085-9641

References

- [1] Wang N C, Sinha S, Cline B, English C D, Yeric G and Pop E 2017 Replacing copper interconnects with graphene at a 7-nm node 2017 IEEE International Interconnect Technology Conference (IITC) 1–3
- [2] Debroy S, Sivasubramani S, Vaidya G, Acharyya S G and Acharyya A 2020 Temperature and size effect on the electrical properties of monolayer graphene based interconnects for next generation mqca based nanoelectronics Sci. Rep. 10 6240
- [3] Thomas S 2018 CMOS-compatible graphene Nat. Electron. 1 612-612
- [4] Jiang J, Kang J, Cao W, Xie X, Zhang H, Chu J H, Liu W and Banerjee K 2017 Intercalation doped multilayer-graphene-nanoribbons for next-generation interconnects *Nano Lett.* 17 1482–8
- [5] Li X et al 2009 Ruoff. Large-area synthesis of high-quality and uniform graphene films on copper foils Science 324 1312-4
- [6] Kim K S et al 2009 Large-scale pattern growth of graphene films for stretchable transparent electrodes Nature 457 706
- [7] Reina A, Jia X, Ho J, Nezich D, Son H, Bulovic V, Dresselhaus M S and Kong J 2009 Large area, few-layer graphene films on arbitrary substrates by chemical vapor deposition *Nano Lett.* 9 30–5
- [8] Yasaei P, Fathizadeh A, Hantehzadeh R, Majee A K, El-Ghandour A, Estrada D, Foster C, Aksamija Z, Khalili-Araghi F and Salehi-Khojin A 2015 Bimodal phonon scattering in graphene grain boundaries *Nano Lett.* 15 4532–40
- [9] Hao Y et al 2013 The role of surface oxygen in the growth of large single-crystal graphene on copper Science 342 720–3
- [10] Chen X, Zhao P, Xiang R, Kim S, Cha J, Chiashi S and Maruyama S 2015 Chemical vapor deposition growth of 5 mm hexagonal singlecrystal graphene from ethanol Carbon 94 810–5
- [11] Bae Set al 2010 Roll-to-roll production of 30-inch graphene films for transparent electrodes Nat. Nanotechnol. 5 574–8
- [12] Ferreira A, Xu X, Tan C-L, Bae S-K, Peres N M R, Hong B-H, Ózyilmaz B and Neto A H C 2011 Transport properties of graphene with one-dimensional charge defects EPL 94 28003
- [13] Gargiulo F and Yazyev O V 2014 Topological aspects of charge-carrier transmission across grain boundaries in graphene Nano Lett. 14
- [14] Vancsó P, Márk GI, Lambin P, Mayer A, Kim Y-S, Hwang C and Biró LP 2013 Electronic transport through ordered and disordered graphene grain boundaries Carbon 64 110
- $[15] Clark K W, Zhang X-G, Vlassiouk I V, He G, Feenstra R M and Li A-P 2013 Spatially resolved mapping of electrical conductivity across individual domain (grain) boundaries in graphene {\it ACS Nano 77956-66}$
- [16] Zhang Y H et al 2014 The distribution of wrinkles and their effects on the oxidation resistance of chemical vapor deposition graphene Carbon 70 81–6
- [17] Mataré HF 1983 Transport processes at grain boundaries in polycrystalline material under optical illumination J. Appl. Phys. 54 6452-8
- [18] Huang PY et al 2011 Grains and grain boundaries in single-layer graphene atomic patchwork quilts Nature 469 389-92
- [19] Tsen A W, Brown L, Levendorf M P, Ghahari F, Huang P Y, Havener R W, Ruiz-Vargas C S, Muller D A, Kim P and Park J 2012 Tailoring electrical transport across grain boundaries in polycrystalline graphene *Science* 336 1143–6
- [20] Koepke J C, Wood J D, Estrada D, Ong Z-Y, He K T, Pop E and Lyding J W 2013 Atomic-scale evidence for potential barriers and strong carrier scattering at graphene grain boundaries: A scanning tunneling microscopy study ACS Nano 775–86

- [21] Grosse K L, Dorgan V E, Estrada D, Wood J D, Vlassiouk I, Eres G, Lyding J W, King W P and Pop E 2014 Direct observation of resistive heating at graphene wrinkles and grain boundaries *Appl. Phys. Lett.* 105 143109
- [22] Isacsson A, Cummings A W, Colombo L, Colombo L, Kinaret J M and Roche S 2017 Scaling properties of polycrystalline graphene: a review 2D Mater 4 012002
- [23] Yu Q et al 2011 Control and characterization of individual grains and grain boundaries in graphene grown by chemical vapour deposition Nat. Mater. 10 443–9
- [24] Jauregui LA, Cao H, Wu W, Yu Q and Chen Y P 2011 Electronic properties of grains and grain boundaries in graphene grown by chemical vapor deposition *Solid State Commun.* 151 1100–4
- [25] Fan X, Wagner S, Schädlich P, Speck F, Kataria S, Haraldsson T, Seyller T, Lemme M C and Niklaus F 2018 Direct observation of grain boundaries in graphene through vapor hydrofluoric acid (vhf) exposure Sci. Adv. 4
- [26] Kang J, Lee C-J, Kim J, Park H, Lim C, Lee J, Choi M and Park H 2019 Effect of copper surface morphology on grain size uniformity of graphene grown by chemical vapor deposition *Curr. Appl. Phys.* 19 1414–20
- [27] Kim K, Lee Z, Regan W, Kisielowski C, Crommie M F and Zettl A 2011 Grain boundary mapping in polycrystalline graphene ACS Nano
- [28] Lee G-H et al 2013 High-strength chemical-vapor-deposited graphene and grain boundaries Science 340 1073-6
- [29] Perera D and Rohrer J 2018 Structure sensitivity of electronic transport across graphene grain boundaries Phys. Rev. B 98 155432
- [30] Yazyev O V and Louie S G 2010 Electronic transport in polycrystalline graphene Nat. Mater. 9 806-9
- [31] Dechamps S, Nguyen V-H and Charlier J-C 2018 Ab initio quantum transport in polycrystalline graphene Nanoscale 10 7759–68
- [32] Majee A K, Foss C J and Aksamija Z 2017 Impact of mismatch angle on electronic transport across grain boundaries and interfaces in 2D materials Sci. Rep. 7 16597
- [33] Chen G 2005 Nanoscale Energy Transport and Conversion Ist edn (New York, NY: Oxford)
- [34] Ophus C, Shekhawat A, Rasool H and Zettl A 2015 Large-scale experimental and theoretical study of graphene grain boundary structures *Phys. Rev.* B 92 205402
- [35] Goodnick S M, Ferry D K, Wilmsen C W, Liliental Z, Fathy D and Krivanek O L 1985 Surface roughness at Si(100)-SiO₂ interface Phys. Rev. B 32 8171–86
- [36] Persson B N J 2001 Theory of rubber friction and contact mechanics J. Chem. Phys. 115 3840-61
- [37] Krim J and Palasantzas G 1995 Experimental observations of self-affine scaling and kinetic roughening at sub-micron length scales *Int. J. Mod. Phys.* B 09 599–632
- [38] Pelliccione M and Lu T-M 2008 Self-Affine Surfaces. In: Evolution of thin film morphology Materials Science CVIII edn (New York, NY: Springer)
- [39] Persson B N J 2014 On the fractal dimension of rough surfaces Tribol. Lett. 54 99-106
- [40] Giannozzi P et al 2009 Quantum espresso: a modular and open-source software project for quantum simulations of materials J. Phys. Condens. Matter 21 395502
- [41] Gilat G and Raubenheimer L J 1966 Accurate numerical method for calculating frequency-distribution functions in solids Phys. Rev. 144 390–5
- [42] Aksamija Z and Knezevic I 2014 Lattice thermal transport in large-area polycrystalline graphene Phys. Rev. B 90 035419
- [43] Nouri N, Ziaei-Rad V and Ziaei-Rad S 2013 An approach for simulating microstructures of polycrystalline materials Comput. Mech. 52 181–92
- [44] Tapasztó L, Nemes-Incze P, Dobrik G, Jae Yoo K, Hwang C and Biró L P 2012 Mapping the electronic properties of individual graphene grain boundaries Appl. Phys. Lett. 100 053114
- [45] Smits F M 1958 Measurement of sheet resistivities with the four-point probe Bell Sys. Tech. 37 711-8